NASA/TM–20210026232

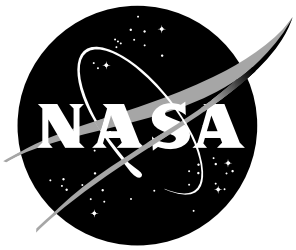

# Characterization of Rochon Prisms for Bi-Directional Imaging Applications

*Joshua M. Weisberger and Brett F. Bathel*
*Langley Research Center, Hampton, Virginia*

January 2022

**NASA STI Program Report Series**

Since its founding, NASA has been dedicated to the advancement of aeronautics and space science. The NASA scientific and technical information (STI) program plays a key part in helping NASA maintain this important role.

The NASA STI Program operates under the auspices of the Agency Chief Information Officer. It collects, organizes, provides for archiving, and disseminates NASA's STI. The NASA STI Program provides access to the NASA Aeronautics and Space Database and its public interface, the NASA Technical Report Server, thus providing one of the largest collection of aeronautical and space science STI in the world. Results are published in both non-NASA channels and by NASA in the NASA STI Report Series, which includes the following report types:

- TECHNICAL PUBLICATION. Reports of completed research or a major significant phase of research that present the results of NASA programs and include extensive data or theoretical analysis. Includes compilations of significant scientific and technical data and information deemed to be of continuing reference value. NASA counterpart of peer-reviewed formal professional papers, but having less stringent limitations on manuscript length and extent of graphic presentations.
- TECHNICAL MEMORANDUM. Scientific and technical findings that are preliminary or of specialized interest, e.g., quick release reports, working papers, and bibliographies that contain minimal annotation. Does not contain extensive analysis.
- CONTRACTOR REPORT. Scientific and technical findings by NASA-sponsored contractors and grantees.
- CONFERENCE PUBLICATION. Collected papers from scientific and technical conferences, symposia, seminars, or other meetings sponsored or co-sponsored by NASA.
- SPECIAL PUBLICATION. Scientific, technical, or historical information from NASA programs, projects, and missions, often concerned with subjects having substantial public interest.
- TECHNICAL TRANSLATION. English-language translations of foreign scientific and technical material pertinent to NASA's mission.

Specialized services also include organizing and publishing research results, distributing specialized research announcements and feeds, providing information desk and personal search support, and enabling data exchange services.

For more information about the NASA STI Program, see the following:

- Access the NASA STI program home page at `http://www.sti.nasa.gov`
- Help desk contact information: `https://www.sti.nasa.gov/sti-contact-form/` and select the "General" help request type.

NASA/TM–20210026232

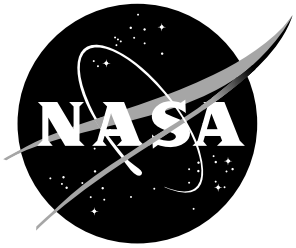

# Characterization of Rochon Prisms for Bi-Directional Imaging Applications

*Joshua M. Weisberger and Brett F. Bathel*
*Langley Research Center, Hampton, Virginia*

National Aeronautics and
Space Administration

Langley Research Center
Hampton, Virginia 23681-2199

January 2022

## Acknowledgments

The authors would like to thank Robert Ren and colleagues at United Crystals for fabrications of the Rochon prisms used in this study. The work was funded by the Plume Surface Interaction (PSI) project and the Transformational Tools and Technologies (TTT) project.



Available from:

NASA STI Program / Mail Stop 148
NASA Langley Research Center
Hampton, VA 23681-2199
Fax: 757-864-6500

## Abstract

Polarizing prisms are often used in applications where light is split into two separate beams of orthogonal polarization, or to isolate a beam with a preferred polarization state. These prisms are typically used with lasers, but there are applications of their use with imaging systems. One such example is that of a recently developed focusing schlieren system, where light must be transmitted through a Rochon prism in both the forward and backward directions. Three Rochon prisms were characterized in this study in terms of their transmitted intensity and polarization state: a quartz/quartz prism, a glass/quartz prism, and a $MgF_2/MgF_2$ prism. Laser testing at four wavelengths was performed, along with full clear aperture collimated LED light testing at a single wavelength. The glass/quartz and $MgF_2/MgF_2$ prisms operated in the same manner when light was transmitted in either the forward or backward direction. The quartz/quartz prism, however, exhibited differences between operation in the forward and backward direction. In the forward orientation for input plane polarized light, the transmitted intensity varied sinusoidally as a function of height of incidence through the prism, while the polarization of the unrefracted and refracted beams were uniform and orthogonally polarized. In the backward orientation, the intensity for both unrefracted and refracted beams was uniform, but the azimuthal orientation of the output plane polarized light varied sinusoidally as a function of height of incidence through the prism, while remaining orthogonally polarized between the two beams at each position.

## 1 Introduction

Polarizing prisms are widely used for optical applications in which the incident light to the prism must be split into two orthogonally polarized beams, which can then be blocked/reflected from the system or used for further analysis. Nicol and Glan-type (Foucault, Thompson, Taylor) prisms transmit one of the rays while internally reflecting the other, isolating a beam with a single polarization. Beam displacers, typically constructed from calcite, are used to laterally displace two beams of orthogonal polarization, both exiting the prism parallel to each other. Wollaston and Nomarski prisms are used to refract both output beams by opposite angles about the prism's optical axis, where the Wollaston prism splits the beams exiting the prism and the Nomarski prism first crosses the beams some distance from the prism's exit face. Rochon and Sénarmont prisms transmit one beam undeviated, while the other is refracted relative to the first beam. Further information on prism types and their uses can be found in [1].

While polarizing prisms are used extensively with laser systems, they have also seen use in imaging applications. Perhaps the most well-known use of polarizing prisms in imaging applications is that of differential interference contrast (DIC) microscopy, where Wollaston and Nomarski prisms are often used [2–4], but Sanderson prisms have also been recently implemented [5]. Another common application of polarizing prisms for imaging is for schlieren interferometry. In this technique, both Wollaston prisms [6, 7] and Sanderson prisms (for sensitivity adjustment) [8–10] are

common.

A focusing schlieren system that implements both a Rochon prism and polarizing beamsplitter, and which only requires the use of a single source/cutoff grid was detailed by Bathel and Weisberger [11]. The benefit of this system is that a matching cutoff grid need not be fabricated to precisely match that of the source grid, which has historically been the most time-consuming aspect of the focusing schlieren system setup [12, 13]. The baseline system in [11] makes use of a quartz/quartz Rochon prism, where light is transmitted through the prism in both the forward and backward directions. In this system, the light passing through the Rochon prism in the backward direction is used to project an image of the grid onto a retroreflective background and experiences no refraction. Upon retroreflection, the light is re-imaged by the system and passes through the Rochon prism in the forward direction, and is refracted by a small angle relative to the instrument's optical axis before an image of the projected grid is made incident on the original grid element. This small angle results in an offset between the original grid and the image of the projected grid. By moving the position of the Rochon prism relative to the original grid, different levels of cutoff of the projected grid can be achieved, which result in varying levels of sensitivity similar to the knife edge adjustment of a conventional schlieren system [14].

The Rochon prism in [11] was chosen for its ability to allow one polarization to transmit through the prism undeviated, while the orthogonal polarization is refracted by a small angle (similarly, a Sénarmont prism could have been used). The magnitude of this angle depends on the crystalline materials used to construct the prism, structure angle ($\alpha$), and wavelength of light transmitted through the prism ($\lambda$). Because polarizing prisms (such as the Rochon prism) are generally used with light propagating through in only one direction, there are few references devoted to the topic of light transmission in the reverse direction, which note that these prisms do not operate in the same manner in both the forward and backward directions (e.g., [15–17]). Further, few, if any, references exist that describe the use of such polarizing prisms for imaging applications where the full clear aperture of a large-diameter prism is used, as most applications involve either the manipulation of light of small-diameter laser beams or microscopic imaging (such as in DIC). During initial testing with a quartz/quartz Rochon prism in the focusing schlieren system, differences between the transmission characteristics of the prism when light was passed in either the forward or backward direction were observed, including spatially-varying intensities and polarization states across the clear aperture of the optic. These observations provided motivation for the work described in this paper, which is to provide a comprehensive understanding of the transmission characteristics of a Rochon prism when used in imaging applications that require light transmission in both the forward and backward directions.

Two distinct measurements are made in this paper to characterize how the Rochon prism performs in laser transmission and imaging applications when light is transmitted in the forward and backward directions. The first measures the output intensity and polarization state of light from four laser sources (blue at 403.5 nm, green at 516.5 nm and at 532 nm, and red at 638.9 nm) as a function of incidence height through the prism. The second uses LED light at 630 nm collimated to a

diameter of 101.6 mm which is transmitted through the prism to evaluate the intensity and polarization of transmitted light over the entire clear aperture. Results from these two tests for the quartz/quartz Rochon prism in the forward orientation are discussed in Section 3.1, and for the backward orientation in Section 3.2. The performance of two Rochon polarizing prisms fabricated with alternative materials, one of glass and quartz and the other entirely of magnesium fluoride, are characterized and compared with the performance of the quartz/quartz polarizing Rochon prism in Section 4. Finally, the use of this prism applied to the projection of a Ronchi ruling for a focusing schlieren system is discussed in Section 5, along with a discussion of the benefits and drawbacks associated with their use in imaging applications.

# 2 Experimental Setup

## 2.1 Rochon Prisms

Three Rochon prisms (RP) are used in this study, each fabricated from two equally-sized, right triangular halves[1] that are cemented together at an angled interface (using Norland Optical Adhesive 61, $n = 1.56$), with nominal structure angle $\alpha$ between the bottom/top face and the interface. The first prism is made from two quartz halves (RP-QQ, $\alpha = 46.5°$), the second from one half glass and the other half quartz (RP-GQ, $\alpha = 76.0°$), and the third from two magnesium fluoride ($MgF_2$) halves (RP-MM, $\alpha = 79.0°$). Schematics and corresponding images of the three prisms can be seen in Fig. 1, with the incident ray denoted by a black arrow, and the unrefracted and refracted rays denoted by green and purple arrows, respectively. The height of the beam incident on the prism, $h$, is measured from the center of the laser beam spot to the bottom of the prism. The *prism axis* is defined here as the axis intersecting the center of face A and face B at normal incidence. The *forward* orientation of the prism refers to applications where light first passes through the prism half with its optic axis aligned with the prism axis, or the glass half for the RP-GQ (initially incident on face A). The *backward* orientation of the prism refers to applications where light first passes through the prism half with its optic axis orthogonal to the prism axis and parallel to the interface plane (initially incident on face B). In the schematics of Fig. 1, the prisms are shown operating in the forward orientation.

The RP-QQ measures 50 mm cubed, and the birefringent quartz has an ordinary and an extraordinary index of refraction of $n_o = 1.54270$ and $n_e = 1.55175$ (at 630 nm), respectively, computed with the Sellmeier relation in [18] used by the prism manufacturer (United Crystals). In prism half A, light is transmitted such that its propagation direction is aligned parallel to the optic axis of the quartz material, denoted with a black line at the bottom right of the prism in Fig. 1(a). In prism half B, the optic axis of the quartz material is oriented orthogonal to the direction of propagation of light and parallel to the interface plane, denoted with a

[1] In reality, the halves are trapezoids, with one of the base lengths being very small to avoid chipping of the material during fabrication.

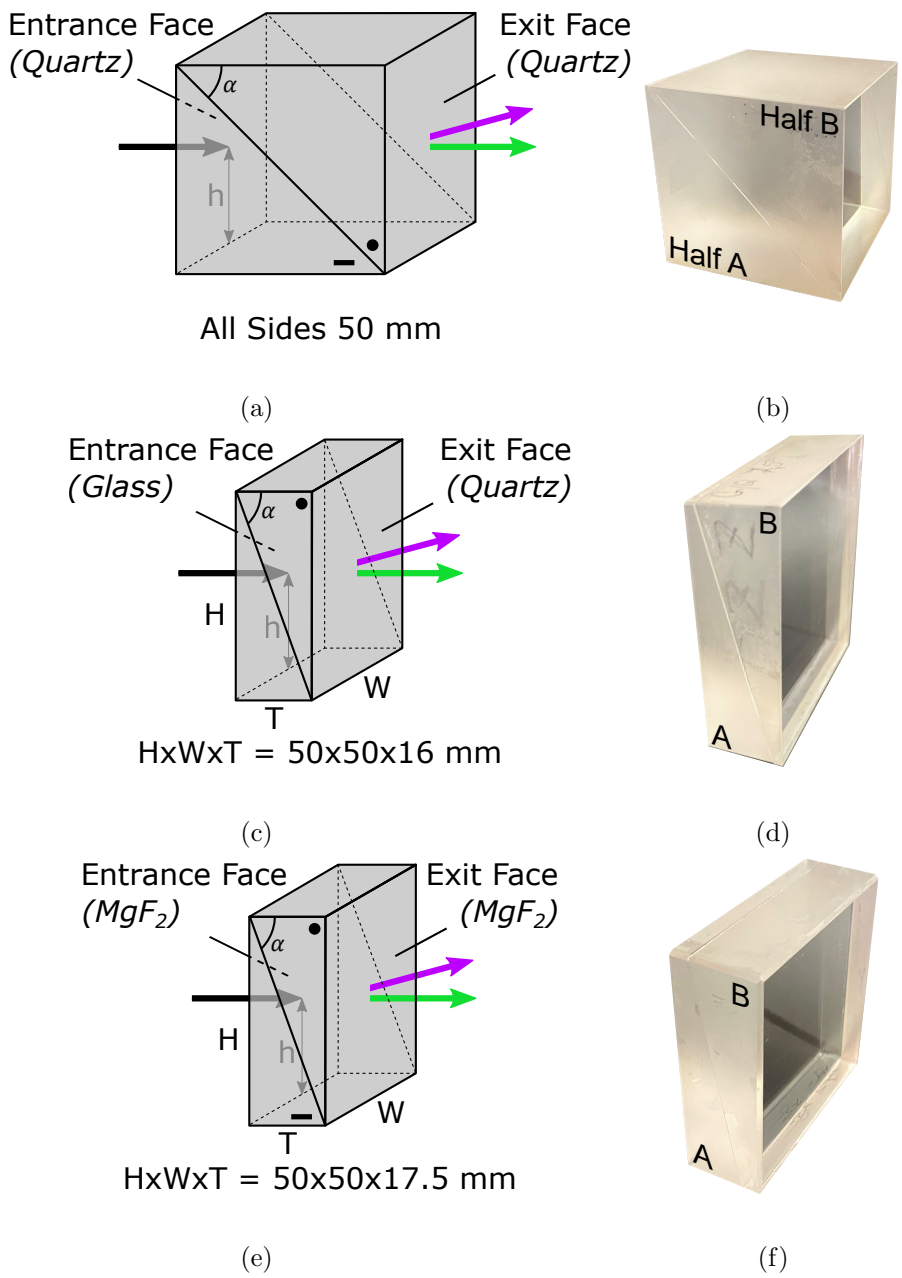


Figure 1: Schematics (a,c,e) and images (b,d,f) of the quartz/quartz (a,b), glass/quartz (c,d), and $MgF_2/MgF_2$ (e,f) Rochon prisms. Light is shown propagating through the prisms in the forward direction.

black circle at the bottom right of the prism. Any refracted light from this Rochon prism (purple arrow) is angled nominally at 30 arc minutes with respect to the prism axis, and in a plane parallel to the sides of the prism. A 7.5 arc minute RP-QQ was also constructed for this study to determine how $\alpha$ modified prism performance. Details of this study are discussed briefly in Section 3.

In the glass/quartz prism RP-GQ (schematic in Fig. 1(c)), an isotropic index-matched glass ($n = 1.54566$) replaces the half A quartz material, as suggested by Ammann and Massey [15]. Due to the small mismatch between the glass index of refraction and the quartz ordinary ray index of refraction ($\Delta n = 0.003$ at $\lambda = 630$ nm), the typically unrefracted ray exiting the prism will in fact be refracted very slightly; a wavelength of $\lambda = 556$ nm is required for an exact index match. The prism was constructed with a clear aperture of $50 \times 50$ mm, a nominal splitting angle of 7.5 arc minutes, and a resulting thickness of 16 mm.

The $MgF_2/MgF_2$ prism RP-MM (schematic in Fig. 1(e)) is constructed of the same material for both halves, and as with the RP-QQ prism, the unrefracted ray is exactly unrefracted. The ordinary and extraordinary index of refraction are $n_o = 1.37703$ and $n_e = 1.38881$ (at $\lambda = 630$ nm), respectively, computed using the Sellmeier relation in [19]. This prism again has a clear aperture of $50 \times 50$ mm and a nominal splitting angle of 7.5 arc minutes, while the thickness is 17.5 mm.

### 2.2 Laser Measurements

In the first experiment, the intensity and polarization transmission characteristics of the Rochon prisms in both the forward and backward orientations were examined using linearly polarized laser light sources. The experimental setup for this test is shown in the schematic of Fig. 2. The light from a $\lambda = 532$ nm laser light source (Spectra Physics, Excelsior 532 Single Mode) first passes through a variable polarizing beamsplitter (PBS) (Thorlabs, VA5-532) which performs two functions: first, it acts as a variable attenuator to control the transmitted laser power using the half-wave plate ($HWP^1$), and second, it ensures the polarization state of the transmitted beam is linearly vertically polarized. Because the extinction ratio of the PBS is not adequate for these measurements ($3 \times 10^3$:1), a linear polarizer (LP) (Thorlabs, LPVISA100-MP2) is used to ensure the highest quality linear vertical polarization state is achieved ($3 \times 10^6$:1). A half-wave plate ($HWP^2$) (Thorlabs, WPH10M-532) is then used to rotate the linear vertical polarization to any linear polarization orientation between horizontal and vertical states, allowing for precise control over the input to the RP. This half-wave plate was mounted to a motorized rotation stage (Thorlabs, K10CR1) to enable precise and repeatable adjustment of its fast axis. The RP is placed in either the forward (Fig. 2(a)) or the backward (Fig. 2(b)) orientation, and is fixed to a pedestal on a motorized vertical translation stage (Thorlabs, MTS50-Z8) to obtain measurements at varying heights of the laser through the prism. The two beams that exit the prism, one unrefracted and one refracted, are then analyzed by a polarimeter (Thorlabs, PAX1000VIS) that was mounted to a motorized translation stage (Thorlabs, MTS25-Z8) to repeatably move back and forth between beam positions. The descriptor of the measured beam can be seen at the right of each schematic, where 'F' denotes the forward orientation, 'B' the backward orientation, 'U' the unrefracted beam, and 'R' the refracted beam. The data acquisition system was automated to ensure the highest accuracy and precision of the measurements.

To quantify how the measured values change with wavelength, three additional laser wavelengths are used: 403.5 nm (Thorlabs, PL205), 516.5 nm (Thorlabs,

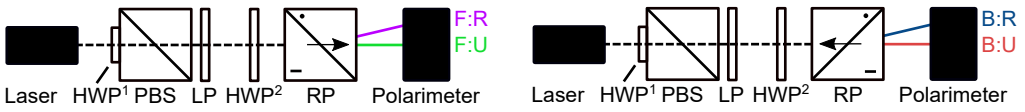


(a) (b)

Figure 2: Laser testing schematics for the (a) [F]orward and (b) [B]ackward orientation of the quartz Rochon prism, with [U]nrefracted and [R]efracted rays labeled.

PL201), and 638.9 nm (Thorlabs, PL202). The output power of these lasers is lower than that of the 532 nm laser, and so the HWP$^1$/PBS attenuator is removed from the system of Fig. 2. The LP mentioned previously is replaced with a broadband linear polarizer (Edmund Optics, #470316, $400-700$ nm) to operate over the range of the three wavelengths used here. Only linearly-vertically polarized light is used for the measurements with these lasers, so the LP is oriented with its transmission axis vertical, and the HWP$^2$ is removed from the system. To achieve maximum transmitted intensity for these lower power lasers, their output linear polarization state is aligned with the transmission axis of the LP.

The polarization state of light is described using the azimuth and ellipticity of the polarization ellipse. The azimuth is defined as the angle between the major axis of the polarization ellipse and the $x$ axis (when light propagates along the $z$ direction). The ellipticity is then calculated as the inverse tangent of the ratio of the semi-minor axis to the semi-major axis dimensions, with a range between $\pm 45°$. When the ellipticity is positive, the light is right-handed, when it is zero, the light is linearly polarized, and when it is negative, the light is left-handed. At $\pm 45°$, the light is circularly polarized, whereas at values between $0°$ and $\pm 45°$, the light is elliptically polarized. With an ellipticity of $0°$, when the azimuth is $0°$, the light is linearly-horizontally polarized (LHP), whereas when the azimuth is $\pm 90°$, the light is linearly-vertically polarized (LVP).

### 2.3 Collimated Light Measurements

To qualitatively validate the laser test data obtained from the experimental setup of Fig. 2, an imaging system is used comprising a large collimated beam of light from a 630 nm LED source (Lightspeed Technologies, HPLS-36DD18B) to fully encompass the clear aperture of the RP. Schematics of the system for both the forward and backward orientations of the RP are shown in Fig. 3(a) and Fig. 3(b), respectively. While light from the LED is initially unpolarized, it is directed through a linear polarizer (LP$^1$) (Edmund Optics, #47-316) to linearly polarize the light in any azimuthal orientation. The diverging light from the LED is collimated by a 101.6 mm diameter, 500 mm focal length lens (CVI Optics, AAP-500.0-101.6-675), such that the collimated beam's diameter is larger than the 50 mm clear aperture of the RP. The light then passes through the RP in either the forward direction (Fig. 3(a)) or backward direction (Fig. 3(b)), then through an optional second linear polarizer LP$^2$ (American Polarizers, AP38-006T), and is incident on a white viewing screen (Thorlabs, EDU-VS1) located a distance $d$ from the RP, where images are

acquired by a CMOS camera (Basler, acA1920-150um) located slightly off-axis to avoid interference with the projected light. Some components are colored in blue, and are optionally added and removed from the system to highlight certain aspects of the RP's polarization transmission characteristics.

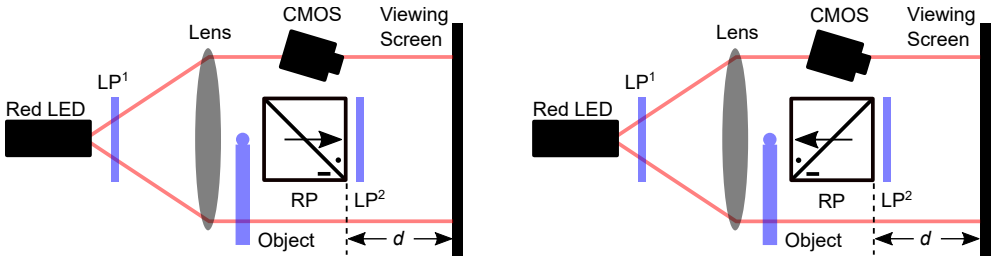


(a) (b)

Figure 3: Collimated LED light testing schematics with Rochon prism oriented in the (a) forward and (b) backward directions. Blue components are optionally included to characterize various aspects of polarization transmission through the RP.

# 3 Quartz/Quartz Rochon Prism

## 3.1 Forward Orientation

The transmitted power using the laser setup of Fig. 2(a) is plotted in Fig. 4 for both the unrefracted (green) and refracted (purple) output beams for varying LVP incident beam heights, $h$. Sub-figures (a) through (c) correspond to data taken with three laser wavelengths: 638.9 nm, 516.5 nm, and 403.5 nm, respectively. For a single input linear polarization state, the output power varies sinusoidally with $h$ (solid fit lines), where the output power for the unrefracted and refracted beams are exactly out-of-phase. The polarization state was also measured for the unrefracted and refracted beams at every vertical position through the RP-QQ; the unrefracted beam exited as LVP light over the entire clear aperture, while the refracted beam exited as LHP light over the entire clear aperture, regardless of the incident beam height on the RP-QQ.

The out-of-phase nature of the unrefracted and refracted beams, and the change in sinusoidal frequency at different light wavelengths in Fig. 4 can be explained using the ray diagrams of Fig. 5. In Fig. 5(a), a single beam is incident normal to the entrance face of the prism with both vertical (line) and horizontal (circle) polarization components. In prism half A, both components travel along, and are orthogonal to, the optic axis. Thus, they both propagate with the same speed as dictated by the ordinary index of refraction, $n_o$, and are called ordinary rays (o-ray). At the angled interface, this beam is split into two separate beams with orthogonal polarization states. The LVP component (green), still orthogonal to the optic axis, continues as an o-ray, unrefracted through the second prism half because there is

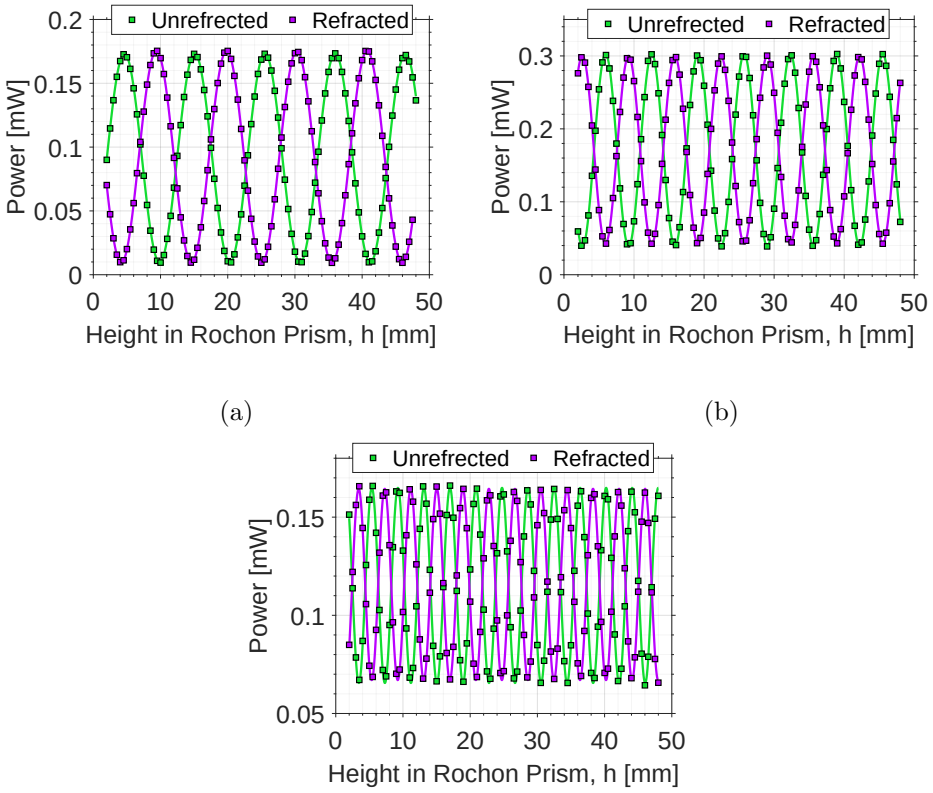


Figure 4: Forward RP-QQ orientation power measured after the RP-QQ for unrefracted (green) and refracted (purple) beams, at various LVP incident beam heights, for laser wavelengths (a) 638.9 nm, (b) 516.5 nm, and (c) 403.5 nm.

no change in index of refraction at the interface. The LHP component (purple) is now parallel to the optic axis in the second prism half, where it becomes the extraordinary ray (e-ray) with its refraction dictated by the extraordinary index of refraction, $n_e$. The parenthetical labeling of the beams indicates their o-ray/e-ray state in prism halves A and B. As quartz is a positive uniaxial crystal, $n_e$ is larger than $n_o$, and in passing through the interface, the LHP beam refracts toward the interface normal. Note that the (o,e) beam is also further refracted at the exit face of the prism, but this is not included in the schematic. There is also a phase difference between the two rays in the second half of the prism, where due to the larger index of refraction, the e-ray propagates more slowly than the o-ray.

When light travels along the optic axis in quartz, it experiences optical activity, in which plane polarized light is rotated azimuthally by the specific rotation, $\rho$ ($^\circ$/mm), which is a function of the wavelength of light. In Fig. 5(b), three LVP rays are incident at different heights in the prism. Due to the different propagation distances through prism half A up to the interface, the azimuthal orientation of the plane polarization of each ray is rotated by a different amount. For example, the

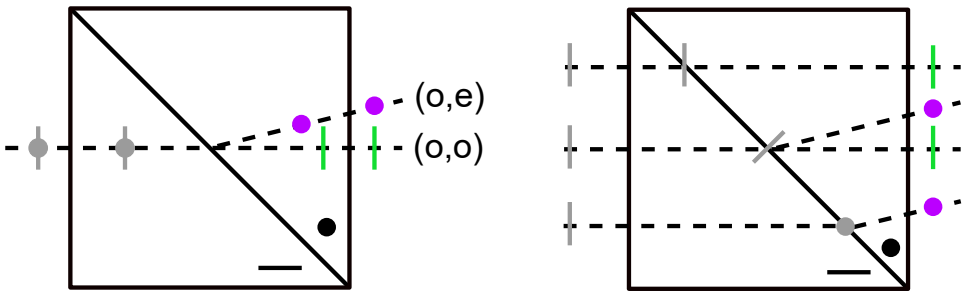


(a) (b)

Figure 5: Ray diagrams of the RP-QQ in the forward orientation (a) for a single ray of light with both vertical and horizontal polarization components (or unpolarized) and (b) for multiple LVP light rays at various incident beam heights.

top ray arrives at the interface as LVP light, the bottom ray as LHP light, and the middle ray as 45° light. The top ray continues fully unrefracted through prism half B, the bottom ray is fully refracted, and the middle ray is split into two orthogonal polarization components, one unrefracted and one refracted. If measuring only the unrefracted beam or only the refracted beam, the power varies sinusoidally over the height of the prism as seen in Fig. 4. Because the specific rotation is larger for shorter wavelengths, the frequency of the oscillation increases for decreasing light wavelengths. This can also be seen in images of a finite diameter laser spot (approximately 3 mm) in Fig. 6 for three wavelengths, where the bottom and top circles are the unrefracted and refracted beams, respectively. From left to right, the height of the incident beam on the entrance face was moved from 2 mm to 10 mm in increments of 0.5 mm, and false-color is used to represent the three wavelengths. For shorter wavelengths (e.g., 403.5 nm), the azimuthal rotation is larger across the diameter of the laser spot, and the dark attenuation band is narrow enough that some of the laser spot is visible even with the band centered on the beam. Conversely, for longer wavelengths (e.g., 638.9 nm), the azimuthal rotation is smaller across the diameter of the laser spot and so the attenuation band is wider, with less of the laser spot visible when the band is centered on one of the beams. The inverse variation of azimuthal rotation with wavelength is discussed in more detail in Section 3.2. These images also demonstrate the out-of-phase nature of the sinusoidal intensity attenuation of both beams; when one beam is attenuated (e.g., refracted), the other beam is not (e.g., unrefracted). Further, if the structure angle, $\alpha$, of the interface were changed, the frequency would again change (a larger structure angle results in lower frequency and vice versa). The images of Fig. 6 also show why the minimum power for the plots in Fig. 4 increases for shorter wavelengths, as the dark attenuation band never fully attenuates either beam. Note that with a smaller laser beam diameter, the minimum power values recorded would approach zero.

The specific rotation of the quartz material can be determined from the plots of Fig. 4. Because the peak power is reached when the interface polarization state is either LVP (for the unrefracted beam) or LHP (for the refracted beam), the po-

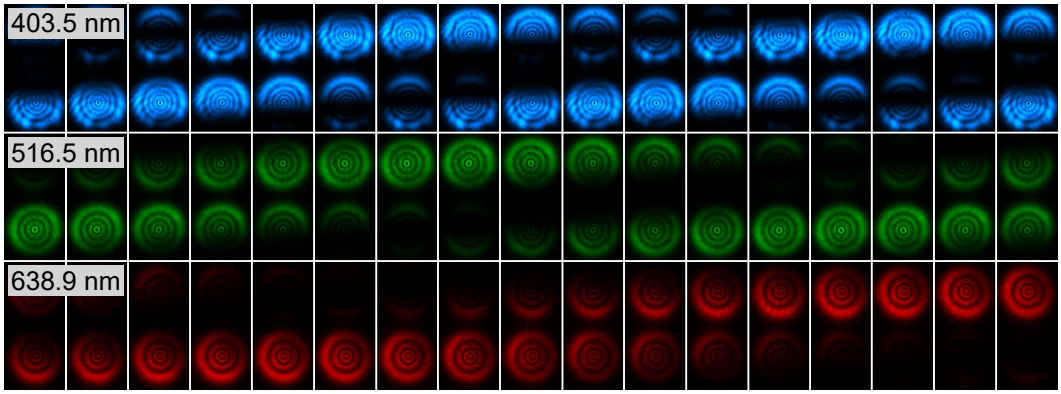


Figure 6: Laser beam images of unrefracted (lower) and refracted (upper) beams for three wavelengths. Attenuation of the beams is a function of the laser spot diameter (approximately 3 mm) and the specific rotation, $\rho$. False-color is used for images to denote the wavelength.

larization azimuth must have rotated 180° from one peak to the next, in either the unrefracted or refracted data. By dividing the difference in prism half A propagation distance (known from the structure angle) by 180°, the specific rotation for each wavelength is obtained: $\rho = 18.14 \pm 0.05$ °/mm at 638.9 nm, $\rho = 28.77 \pm 0.08$ °/mm at 516.5 nm, and $\rho = 48.99 \pm 0.17$ °/mm at 403.5 nm. These values were computed for each wavelength using both the unrefracted and refracted data, and the uncertainty is the $1\sigma$ standard deviation of all the peak-to-peak measurements. Further comparisons of the specific rotation to experimental data and values from existing literature are detailed in Section 3.2.

While only a single polarization state (LVP) incident on the RP-QQ is shown in Fig. 4, tests for other input polarization states were conducted, and indicated that for any incident linear polarization state, both unrefracted and refracted beams are transmitted simultaneously, with the same out-of-phase sinusoidal trend shown in the figure. If circularly polarized (or unpolarized) light is incident, however, the sinusoidal pattern will not be visible because at every beam height, both the unrefracted and refracted beams will be produced with uniform intensity across $h$. From these observations, it is not possible to isolate only the unrefracted or the refracted beam when the RP-QQ is placed in the forward orientation by using only the input polarization state. The out-of-phase relationship of the unrefracted and refracted beams is unique to the laser testing because for each incident beam height, the polarimeter was moved to either the unrefracted or refracted beam position to make the power measurement. Because the refracted beam from the prism is split away from the unrefracted beam at an angle, the projected intensity variation will not be exactly out-of-phase at every position on the viewing screen for the collimated LED light testing.

This is verified using the collimated LED light testing setup shown in Fig. 3(a). The polarization state incident on the RP-QQ was set to LVP using the $LP^1$ for all subsequent images, as other input linear polarizations simply shift the phase of the sinusoidal intensities for both beams over prism's clear aperture. Images for three

viewing screen positions relative to the RP-QQ exit face are shown in Fig. 7: (a) $d =$ 600 mm, (b) $d = 900$ mm, and (c) $d = 1200$ mm. Each image has three sub-images side-by-side. The left image is taken without the $LP^2$, and so is a combined image of the unrefracted and refracted beams on the plate (denoted by C). The middle and right images are taken with the $LP^2$ in the vertically-transmitting (unrefracted, U) and horizontally-transmitting (refracted, R) orientations, respectively. These two beams can be completely isolated with the $LP^2$ because, as measured from the laser test data, each beam is uniformly linearly polarized over the entire clear aperture of the RP-QQ, and both are orthogonally polarized relative to each other.

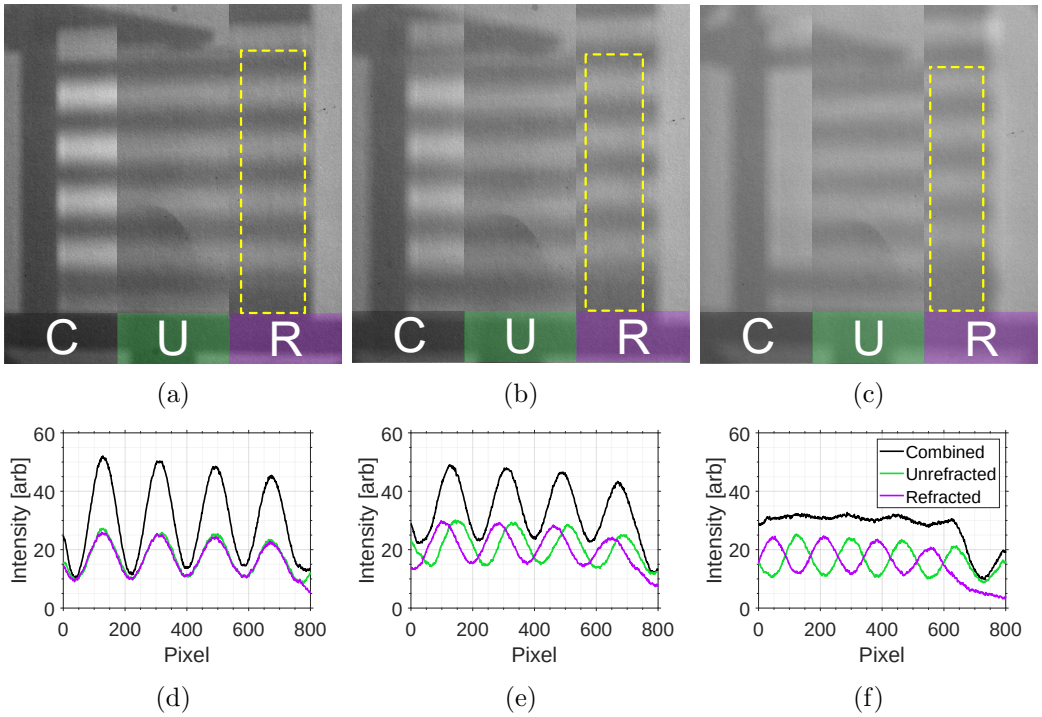


Figure 7: (a-c) Viewing screen images of the intensity without $LP^2$ [C], with $LP^2$ oriented to be vertically-transmitting [U], and with $LP^2$ oriented to be horizontally-transmitting [R]. (d-f) Corresponding plots of vertical profiles for the C, U, and R images, extracted from width-averaged profiles of the dashed yellow boxes.

For the combined, unrefracted, and refracted images for each viewing screen position, a vertical profile was extracted (averaged across the width of the dashed yellow boxes in Figs. 7(a-c)), and the intensity plotted versus the image pixel in Figs. 7(d-f). The extracted profile extends from the bottom to the top of the clear aperture of the prism in the unrefracted image. Both the intensities and pixel numbers are arbitrary, as only qualitative trends are discussed here. Larger pixel values indicate lower positions on the images. Note that a slight crease in the paper fixed to the viewing screen can be seen in the middle sub-images, but the extracted profiles do not include this region. In Figs. 7(a,d), the plate is at a distance ($d = 600$ mm) such that the unrefracted and refracted fringes are exactly aligned, and so the combined profile is highly pronounced as a result of near-total

"constructive" intensity superposition. In Figs. 7(b,e), the viewing screen was moved 300 mm further from the RP-QQ exit ($d$ = 900 mm), and the refracted beam's fringe has shifted higher in the image (lower in pixel-space). The fringe pattern is still visible in the combined image, but the contrast between the bright and dark fringes has noticeably decreased. In Figs. 7(c,f), when the viewing screen is moved a further 300 mm from the RP-QQ exit face ($d$ = 1200 mm), the combined image/plot shows uniform illumination over the entire prism clear aperture. The unrefracted and refracted beams in this instance are exactly out-of-phase, and so their combination produces the uniform illumination, with no visible fringes as a result of near-total "destructive" intensity superposition. The results of this test also allow for the refraction angle of the prism to be verified using the viewing screen separation distance from the RP-QQ and the wavelength of the intensity patterns observed in Figs. 7(a,d) and Figs. 7(c,f). The data of Fig. 4(a) are used, while noting that the wavelength of the laser is slightly different than the LED (638.9 mm vs. 640 nm). The peak separation distance from Fig. 4(a) is 10.45 mm. As the viewing screen was moved from $d$ = 600 mm to $d$ = 1200 mm, the sinusoidal intensity pattern of the refracted beam was shifted by one half of its wavelength, or 5.23 mm. The resulting refraction angle is then $\tan^{-1}(5.23/600) = 0.5°$, comparing favorably to the 30 arc minute splitting angle specified by the manufacturer.

The same test was also performed with the 7.5 arc minute RP-QQ described in Section 2.1 with the resulting frequency of the intensity bands being noticeably lower than those shown in Fig. 7. This reduction in frequency is a consequence of the increased structure angle of the prism, which results in a more slowly varying prism half A propagation distance as a function of beam incidence height, $h$.

There are three key takeaways from this section. The first is that both the unrefracted and refracted beams are always transmitted simultaneously when used in imaging applications where a significant portion of the prism's clear aperture is used to transmit light, regardless of the input polarization state to the prism (or lack thereof). In these imaging situations, it is thus not possible to isolate either of the beams based on the input light's polarization state. The transmitted intensity of the unrefracted and refracted beams varies sinusoidally along the height of the prism if the input beam is plane polarized in any azimuthal direction. The second takeaway is that the polarization state of the unrefracted beam is always LVP, and that of the refracted beam is always LHP, regardless of incident beam height in the prism. The final takeaway is that for input light that is linearly or elliptically polarized, the frequency of the transmitted intensity variation for each beam increases or decreases with decreasing or increasing structure angle, respectively.

### 3.2 Backward Orientation

The orientation of the RP-QQ was reversed to make measurements through the prism in the backward orientation, as shown in Fig. 2(b) for the laser testing and in Fig. 3(b) for the collimated light testing. Transmitted power and polarization data from the laser setup are shown in Fig. 8(a) and Fig. 8(b), respectively, using the 532 nm laser. In Fig. 8(a), the input linear polarization azimuth to the RP-QQ is plotted on the horizontal axis; azimuths between 0° (LHP) and ±90° (LVP) remain

linearly polarized because the HWP$^2$ simply rotates the linear polarization azimuth (ellipticity is 0°). When incoming light to the RP-QQ is LVP, the unrefracted beam is fully transmitted, and no refracted beam is observed. Conversely, when the incoming light is LHP, no unrefracted beam is observed while the refracted beam is fully transmitted. When the incoming beam's azimuth is ±45° (denoted by the vertical dashed lines in Fig. 8(a)), both the unrefracted and refracted beams are equally transmitted because equal parts of vertical and horizontal polarization are present in the incident beam. Transmitted power data were taken at multiple vertical positions through the RP-QQ, and the measured power transmission characteristics remained unchanged. Only two of these vertical positions are plotted in Fig. 8(a) (squares for $h = 2$ mm and triangles for $h = 24$ mm) for clarity, and the solid lines are sinusoidal curve fits to the square data points. This indicates that when light with a single linear polarization state enters the RP-QQ in the backward orientation, the intensity of the unrefracted and/or refracted light exiting the RP-QQ will be uniform over the entire clear aperture.

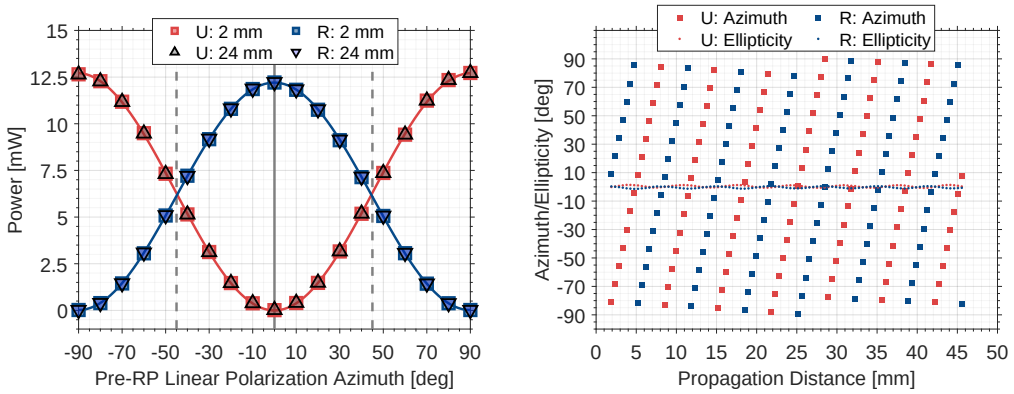


(a) (b)

Figure 8: (a) Power measured after a backward oriented RP-QQ for unrefracted and refracted beams at two incident beam heights, and (b) output linear polarization azimuth/ellipticity as a function of prism half A propagation distance, using a laser wavelength of 532 nm.

The HWP$^2$ was then used to orient the light's polarization state to either LVP (full unrefracted beam transmission) or LHP (full refracted beam transmission). The beam was made incident on face B of the RP-QQ at incremental heights from near the bottom of the prism ($h = 2$ mm) to near the top of the prism ($h = 48$ mm), and using the structure angle of $\alpha = 46.5°$, the propagation distance through each prism half was calculated. The transmitted azimuth and ellipticity are plotted versus the propagation distance of the unrefracted beam in Fig. 8(b), noting that the propagation distance for the refracted beam is actually slightly larger than the unrefracted. The results of this plot can be explained with the help of the ray diagrams of Fig. 9. Three incident LVP light beam heights are shown in Fig. 9(a), and because the polarization is orthogonal to the optic axis in the prism half B, the

beams all propagate as o-rays and arrive at the interface plane as LVP light. In the prism half A, the LVP light beams remain orthogonal to the optic axis, and so continue as o-rays in this half without experiencing any refraction. However, because the light is now traveling along the optic axis, the linear polarization azimuth is rotated by the specific rotation of the quartz due to optical activity. The azimuthal angle of each beam as it reaches face A is a function of the propagation distance through prism half A and the wavelength of light. A similar phenomenon occurs for input LHP light (Fig. 9(b)), except that in prism half B, the LHP light is parallel to the optic axis and is an e-ray. In prism half A, these beams become o-rays, and so are refracted away from the interface normal ($n_o > n_e$). These beams also experience optical activity because they have a component of travel along the optic axis. The linear variation of the output polarization azimuth in Fig. 8(b) for both the unrefracted and refracted data is a result of this optical activity over the entire clear aperture of the prism. The specific rotation, $\rho$, is determined using a linear regression for each segment of data, and for both the unrefracted and refracted beams, $\rho = 26.77 \pm 0.06$ °/mm, where the uncertainty is computed as the standard deviation ($1\sigma$) of all the linear regressions. This value compares favorably to that of Jenkins and White [17], where for quartz at 532 nm, $\rho$ is interpolated to be approximately 27.1 °/mm. The consequence of these results is that while the exiting intensity from the backward oriented RP-QQ is uniform for either the unrefracted or refracted beam, the output polarization state varies as a function of propagation distance through the prism half A, and thus the linear polarization azimuth over the height of the prism constantly changes.

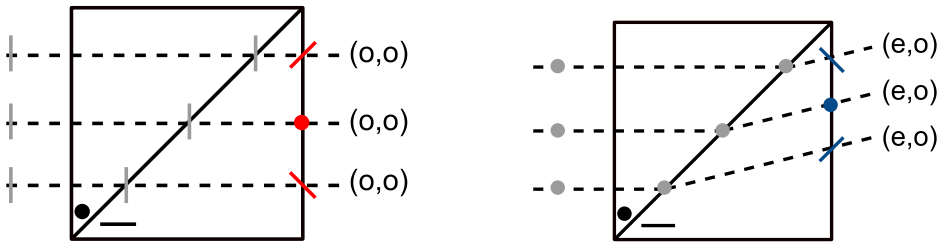


(a) (b)

Figure 9: Ray diagrams of the RP-QQ in the backward orientation (a) for multiple LVP light rays at various incident beam heights and (b) for multiple LHP light rays at various incident beam heights.

The collimated light testing shown schematically in Fig. 3(b) for the backward orientation is able to qualitatively show the state of polarization transmitted through the RP-QQ over its entire clear aperture, as opposed to a single laser beam with data points from discrete positions. Three images are presented in Fig. 10 for qualitative comparison to the power data from Fig. 8(a), and are obtained by setting the $LP^1$ to three representative azimuthal orientations (0°, 45°, and 90°) and by removing the $LP^2$. The object, a ball-end hex driver, is included to clearly show the unrefracted and refracted behavior of the projected light which forms a silhouette of the object

on the viewing screen. The outer circular edge between the light and dark regions in these images represents the extent of the entire collimated, 101.6 mm diameter beam. Inside this bright region, the optical post and stand used to mount the 50 mm-cube RP-QQ are visible, along with the RP-QQ itself and the ball-end hex driver.

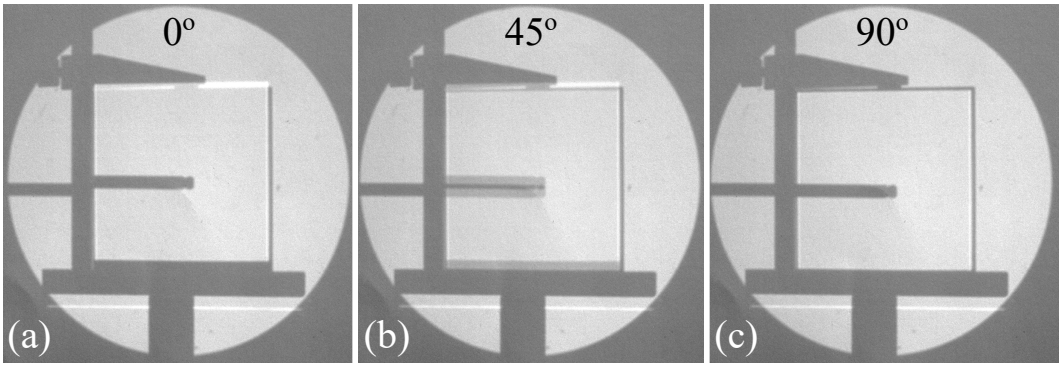


Figure 10: Backward-oriented RP-QQ collimated light images for three azimuthal transmission axes of the $LP^1$. For these images, the $LP^2$ was removed and the ball-end hex driver object was included (see Fig. 3(b)).

When the incident light on prism face B is LHP (0°) as in Fig. 10(a), only the refracted beam is fully transmitted, with uniform intensity over the entire clear aperture. Here, the shadow of the ball-end hex driver through the RP-QQ is refracted upward, and appears fully dark. When the incoming light is LVP (90°) as in Fig. 10(c), only the unrefracted beam is fully transmitted, again with uniform intensity. The shadow of the ball-end hex driver in the image is unrefracted, and is again fully dark. When the incoming light is now azimuthally rotated to 45°, the unrefracted and refracted transmitted light beams have equal intensity, and are both uniform over the clear aperture. The shadow of the ball-end hex driver appears split between the unrefracted and refracted positions, with the bottom shadow from the unrefracted light and the top shadow from the refracted light. In this image, the intensity for the top portion of the refracted shadow and the bottom portion of the unrefracted shadow is observed to have reduced contrast as a result of the oppositely refracted beams being incident on these portions of the respective shadows. In the middle, where the two beams overlap, the shadow of the ball-end hex driver appears fully dark, as no light from either the unrefracted or refracted beam is incident on this region of the viewing screen. Since the refracted light exits the RP-QQ at an angle relative to the unrefracted light, any adjustment of the viewing screen either away from or towards the RP-QQ would result in the shadows being either further separated or more overlapped with one another, respectively.

To qualitatively verify that the output polarization azimuthal angles are rotated as a function of the height of incidence through the backward oriented RP-QQ as shown in Fig. 8(b), the $LP^1$ was set to 90° to transmit LVP light, and the $LP^2$ added to the system at three rotational positions: 90°, 45°, and 0°. All three images are combined in Fig. 11 with the appropriate $LP^2$ angles indicated. The $LP^2$ slightly

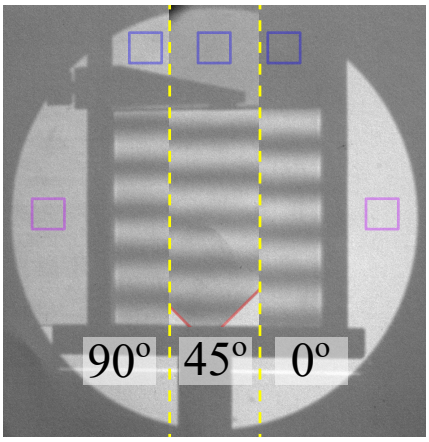


Figure 11: Backward RP-QQ collimated light polarization testing for LVP input light at three azimuthal angles of the $LP^2$, indicated on their respective portion of the image.

attenuates the transmitted light even when aligned with the $LP^1$ at 90°, visible in the intensity difference between the two square purple regions; the light for the right region does not pass through the $LP^2$, while the light for the left region passes through the $LP^2$ oriented at 90°, aligned with the $LP^1$. The orientation of the $LP^2$ is verified by the transmitted intensity on the viewing screen in the blue square regions above the RP-QQ. At 0°, the light is fully attenuated as the $LP^2$ transmission axis is orthogonal to that of $LP^1$. At 90°, the light is fully transmitted (except for the non-ideal attenuation of the polarizer), and at 45°, half the light is transmitted. For the $LP^2$ orientation of 45°, the square polarizer did not encompass the full clear aperture of the RP-QQ, and the bottom corner edge of the polarizer is denoted by the red diagonal lines.

In the three RP-QQ regions of the image (separated by yellow dashed lines), a sinusoidal intensity variation is shifted vertically as the transmission axis of the $LP^2$ is rotated relative to the transmission axis of the $LP^1$. In the unrefracted (red) data of Fig. 8(b), the azimuth of the transmitted light is continuously rotated as a function of the product of the specific rotation and the prism half A propagation distance. The inclusion of the $LP^2$ (in Fig. 11) then serves to filter the transmitted intensity of this output beam, resulting in the observed sinusoidally varying intensity pattern. By rotating the transmission axis of the $LP^2$, the resulting intensity pattern observed on the viewing screen shifts linearly with this angle. This can be visualized by drawing a horizontal line on Fig. 8(b) at the $LP^2$ angle, where the intersection of this line and the azimuthal data correspond to the bright peaks in Fig. 11.

A 532 nm laser was used to acquire the data of Fig. 8(b), while a 630 nm LED was used for the data of Fig. 11. Thus, the number of peaks/troughs (four to five) in the LED sinusoidal intensity variation does not match the number expected from the laser data (seven) due to the strong dependence of the specific rotation on wavelength, referred to as rotary dispersion. Figure 12(a) shows how the specific rotation angle varies with the wavelength of light; a steeper slope indicates a larger

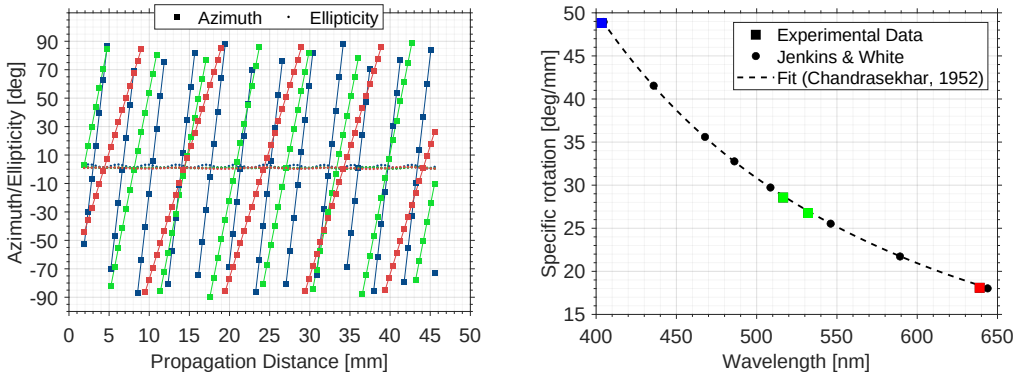


(a) (b)

Figure 12: (a) Azimuth (squares) and ellipticity (dots) as a function of propagation distance through prism half B for three laser colors: blue (403.5 nm), green (516.5 nm), and red (638.9 nm), and (b) plot of specific rotation versus wavelength demonstrating rotary dispersion.

specific rotation, and vice versa. In this figure, only the unrefracted beam was monitored, and the experimental setup of Fig. 2 was altered slightly as discussed in Section 2.2. The three laser wavelengths plotted in Fig. 12(a) are 403.5 nm (blue), 516.5 nm (green), and 638.9 nm (red), and the line fit through each of the appropriate data points has a slope that corresponds to the specific rotation for each wavelength: $\rho = 48.82 \pm 0.08$ °/mm at 403.5 nm, $\rho = 28.56 \pm 0.05$ °/mm at 516.5 nm, and $\rho = 18.09 \pm 0.03$ °/mm at 638.9 nm. These experimentally determined specific rotation data points, including the 532 nm value measured earlier, are plotted versus laser wavelength in Fig. 12(b) with colored squares. Specific rotation values from [17] are plotted with circles, and the fit from [20] is plotted with a dashed line,

$$\rho = \frac{k\lambda^2}{\left(\lambda^2 - \lambda_0^2\right)^2} \tag{1}$$

where $k = 7.186$ and $\lambda_0 = 0.0926283$ $\mu$m. All the data in the figure compare favorably. In the visible wavelength range, the specific rotation's dependence on wavelength can also be approximated by Cauchy's equation [17],

$$\rho = A + B/\lambda^2 \tag{2}$$

where $A$ and $B$ are constants determined here by using a fit of the experimental data at four wavelengths: $A = -2.589$ °/mm and $B = 8.353 \times 10^6$ ° $\cdot$ nm$^2$/mm. This Cauchy fit is not included on the plot of Fig. 12(b) because it very nearly overlaps the fit of [20]. Shorter wavelengths exhibit larger azimuthal polarization rotation angles than longer wavelengths for the same change in propagation distance through prism half A. Consequently, the spatial frequency of the intensity pattern after passing through a linear polarizer (e.g., LP$^2$), similar to that observed in Fig. 11, will increase as the wavelength of transmitted light is decreased. The number

of expected peaks/troughs from the red data points in Fig. 12(a) matches those seen in Fig. 11 (four to five). As mentioned in Section 3.1, when using the 7.5 arc minute RP-QQ with a much larger structure angle than the 30 arc minute RP-QQ, the propagation distance varies more slowly with incidence height, $h$, resulting in a lower frequency of the transmitted polarization azimuth compared to that shown in Fig. 11. As mentioned in Section 3.1, the larger value of $\rho$ for shorter wavelengths helps explain the trends of Fig. 6, where the frequency of the intensity variation is higher for shorter wavelengths due to the faster rotation of the polarization azimuth over the height of the prism. For both forward and backward orientations, the azimuthal rotation takes place in prism half A, which for the forward orientation is the first prism half the beam encounters, whereas for the backward orientation, it is the second prism half the beam encounters.

There are two main takeaways from the backward orientation RP-QQ measurements. The first is that the projected intensity is always uniform, regardless of where the light passes through the prism. For input LVP light, the unrefracted beam is fully transmitted, while for input LHP light, the refracted beam is fully transmitted. For other input polarization states (or unpolarized light), both the unrefracted and refracted beams will be transmitted simultaneously, both with uniform intensity. The second is that the output polarization state of the light remains nearly fully linear, but has a varying azimuthal angle over the height of the prism (but not the width) depending on the total azimuthal specific rotation (°/mm) of the light through prism half A, which is a function of the light's wavelength. The frequency of the azimuthal rotation of polarization decreases with an increase in structure angle due to the smaller change in propagation distance with incidence height, $h$.

# 4 Glass/Quartz and $MgF_2/MgF_2$ Rochon Prisms

Because the light in the prism half A travels in the same direction as the optic axis, it was noted more than a century ago that this half of the prism could instead be made from less expensive, index-matched glass. An angle-measuring device from 1909 used this modified Rochon prism in its design (glass-calcite) [21], and in the late 1960s, a modified Rochon and modified Glan-Thompson prism were proposed (glass-quartz) [15,22,23]. The laser light testing and collimated light testing outlined earlier in Sections 2.2 and 2.3, respectively, were used to evaluate the RP-GQ design and the RP-MM (described in Section 2.1). The RP-MM was fabricated and tested for two reasons. The first is that light traveling through $MgF_2$ does not experience optical activity, and so both halves can be constructed from the material without inducing azimuthal rotation of the polarization state. The second reason relates to one of the minor limitations of the glass-quartz prism, where due to the slight mismatch in the index of refraction of the glass and the quartz, the unrefracted beam will in fact be slightly refracted. For the RP-MM, because both halves are made from the same material, the unrefracted beam is truly unrefracted. The purpose of these tests was to validate the hypothesis that the RP-GQ and RP-MM prisms operate the same in the forward and backward orientations because of the absence

of optical activity in these materials, unlike the RP-QQ described in Section 3.

The laser measurements were performed for the forward and backward orientation at four heights through the prisms using the 532 nm laser: $h = 12$ mm, 22 mm, 32 mm, and 42 mm. For the RP-GQ and the RP-MM in both the forward and backward orientations, when the input polarization was LVP, the output beam was unrefracted and remained LVP light, with uniform intensity over the entire clear aperture. When the input polarization was LHP, the output beam was refracted and remained LHP light, again with uniform intensity over the entire clear aperture. Measurements were only acquired at four distinct locations because when the laser was scanned through the entire height of the prisms, no changes for either the intensity or polarization state were observed (as expected due to the lack of optical activity effects). These laser measurements determine that the RP-GQ and RP-MM operate the same in the forward and backward orientations.

Full clear aperture images for the collimated LED light testing of the RP-GQ and RP-MM are shown in Fig. 13 for both the forward and backward orientations, where sub-figures (a,b,e,f) show the RP-GQ and sub-figures (c,d,g,h) show the RP-MM. For sub-figures (a,c,e,g), $LP^1$ is oriented such that the input light polarization state is LVP, so that only the unrefracted beam exits the prisms, whereas in (b,d,f,h), the input light polarization state is LHP, so that only the refracted beam exits the prisms. The $LP^2$ is not included in the system for these images, but the ball-end hex driver object is, as per the schematic of Fig. 3. The refracted beam images of (b,d,f,h) show the object displaced vertically from its actual position at the left side of the image. The unrefracted beam images of (c,g) show the object in the same vertical position as the actual position. However, in the unrefracted beam images of (a,e), the unrefracted object can in fact be seen to be very slightly refracted downwards, which is a result of the slight mismatch of index of refraction between the glass and quartz materials of the RP-GQ at the LED wavelength of 630 nm. The corresponding images of (a-d) and (e-h) are indistinguishable, verifying that the prisms operate the same in the forward and backward orientations.

The ball-end hex driver object was removed from the system, and the exiting light's intensity and polarization were characterized over the entire clear aperture of the prisms, with resulting composite images shown in Figs. 14(a-d) for the forward orientation and in Figs. 14(e-h) for the backward orientation. Each sub-figure is a composite image of three $LP^2$ states: removed from the system (None), oriented with the transmission axis vertical (Vert), and oriented with the transmission axis horizontal (Horz). Each sub-figure also has a label indicating the orientation of the $LP^1$, which when set to LVP allows only the unrefracted beam to transmit and when set to LHP allows only the refracted beam to transmit, as shown in Fig. 13. The resulting images are indistinguishable for the prisms in both the forward and backward orientations. With incoming LVP light, the unrefracted beam is transmitted with uniform intensity and with uniform LVP polarization state. With incoming LHP light, the refracted beam is transmitted with uniform intensity and with uniform LHP polarization state. The slight intensity attenuation between the appropriate cases with and without the $LP^2$ included is due to absorption of the linear polarizer film being used.

A comparison of the intensity and polarization transmission characteristics of

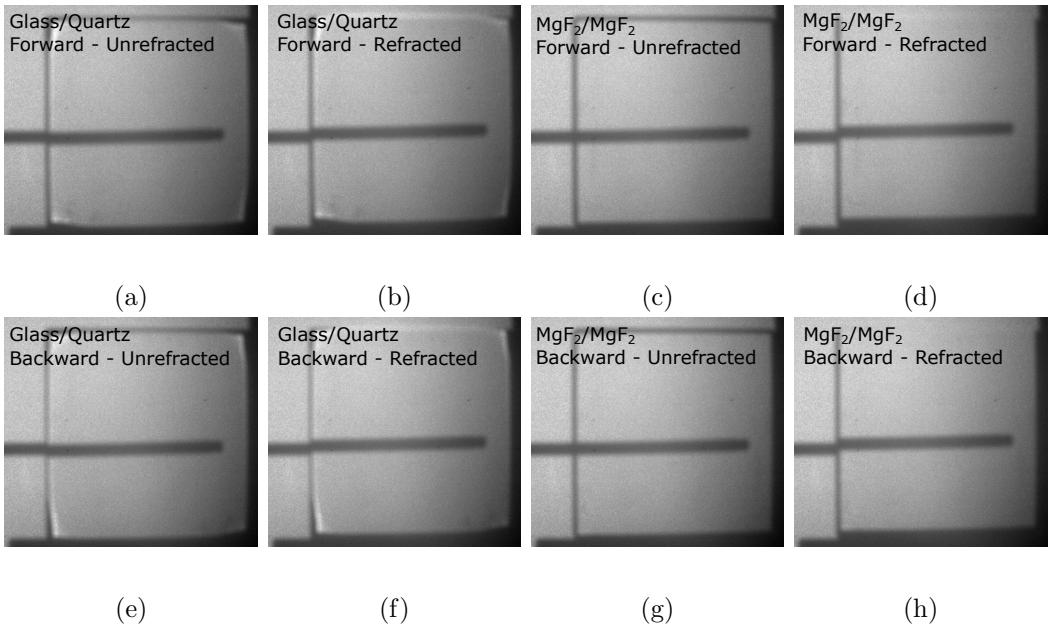


Figure 13: Collimated light testing for (a-d) forward and (e-h) backward orientations, for the (a,b,e,f) RP-GQ and (c,d,g,h) RP-MM, with a ball-end hex driver object to visualize refraction. Input light polarization (using $LP^1$) for the (a,c,e,g) unrefracted images is LVP, and for the (b,d,f,h) refracted images is LHP.

the three prisms in the forward and backward directions for both the unrefracted and refracted beams is shown in Table 1. The RP-GQ and RP-MM operate the same in the forward and backward orientations, and can be used interchangeably for most applications. The only difference between the two is that the unrefracted beam of the RP-GQ has a very small refraction angle at the wavelengths used in this study due to the slight mismatch in index of refraction between the glass and quartz; the unrefracted beam from the RP-MM is exactly unrefracted. The RP-QQ, however, does not operate the same in both orientations; in the forward orientation, the polarization azimuth is uniform while the intensity varies, whereas in the backward orientation the opposite is true, and the polarization azimuth varies while the intensity is uniform.

The key takeaway from the RP-GQ and RP-MM testing is that both prisms operate the same in the forward and backward orientation, as optical activity effects are not present within prism half A for either. In both orientations, the transmitted light intensity for both the unrefracted and refracted beams is uniform over the entire clear aperture (in contrast to the RP-QQ in the forward orientation). Both the unrefracted and refracted beams have a uniform polarization state over the clear aperture upon exiting the prism, with the unrefracted beam exiting as LVP light, and the refracted beam exiting as LHP light.

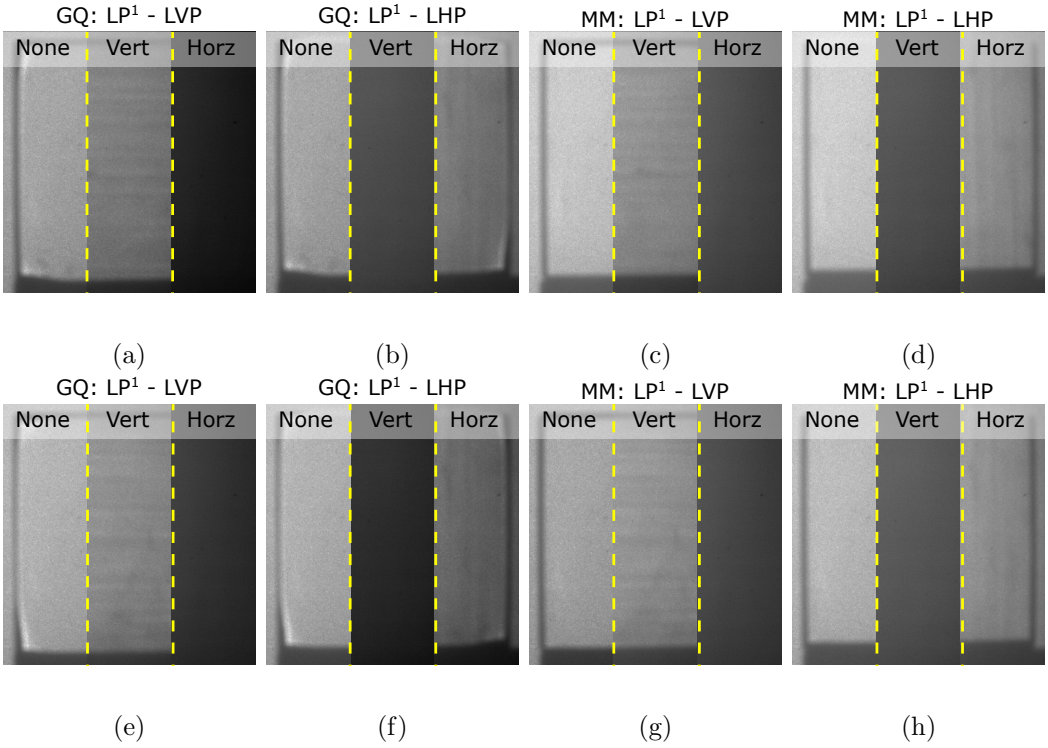


Figure 14: Collimated light testing for (a-d) forward and (e-h) backward orientations, for the (a,b,e,f) RP-GQ and (c,d,g,h) RP-MM. Input light polarization (using $LP^1$) for the (a,c,e,g) unrefracted images is LVP, and for the (b,d,f,h) refracted images is LHP. $LP^2$ inclusion/orientation state is denoted at the top of each composite sub-image.

## 5 Focusing Schlieren Imaging Application

The RP-QQ in the focusing schlieren system of [11] is oriented such that light is projected out of the instrument through the prism in the backward orientation. The system initially transmits light unrefracted through the prism in the backward direction in order to project an image of a Ronchi ruling on a retroreflective background, which is reflected back toward the instrument, eventually passing through the prism in the forward orientation and being refracted by a small angle (nominally 30 arc minutes). The refraction of light from the projected Ronchi ruling is then made incident on the same Ronchi ruling, but at a slight offset, providing a level of cutoff similar to the knife edge cutoff in a conventional schlieren system. It is the magnitude of this cutoff that dictates the sensitivity of the measurement to density disturbances at the instrument's measurement plane. The projected image of the ruling on the background must be sharp to achieve the highest quality focusing capability. A composite image of the projected ruling on the retroreflective background can be seen in Fig. 15 for three input linear polarization states to the RP-QQ when oriented in the backward direction; LHP (0°), ±45°, and LVP (90°). These images were taken with a separate off-axis camera focused on the viewing screen, which

Table 1: Summary of prism operating characteristics for intensity and polarization transmission for the unrefracted/refracted beams, in the forward/backward orientations.

| | | Unrefracted ($LP^1 \rightarrow$ LVP) | | Refracted ($LP^1 \rightarrow$ LHP) | |
|---|---|---|---|---|---|
| Prism | Orientation | Intensity | Polarization | Intensity | Polarization |
| RP-QQ | Forward | Varying | Uniform, LVP | Varying | Uniform, LHP |
| RP-GQ | Forward | Uniform | Uniform, LVP | Uniform | Uniform, LHP |
| RP-MM | Forward | Uniform | Uniform, LVP | Uniform | Uniform, LHP |
| RP-QQ | Backward | Uniform | Varying | Uniform | Varying |
| RP-GQ | Backward | Uniform | Uniform, LVP | Uniform | Uniform, LHP |
| RP-MM | Backward | Uniform | Uniform, LVP | Uniform | Uniform, LHP |

here is a retroreflective material, and are similar in nature to the images of Fig. 10.

Sharp opaque grid lines of the Ronchi ruling are seen for both LHP (0°) and LVP (90°) incident light through the backward oriented RP-QQ. From Fig. 8(a), with an input polarization azimuth of LVP, only the unrefracted light is transmitted, and conversely, with an input polarization azimuth of LHP, only the refracted light is transmitted. The projected grid for the LHP case was observed to be refracted slightly upwards from the unrefracted LVP case projected grid. At an input polarization azimuth of ±45°, both the unrefracted and refracted beams are transmitted equally. These two projected grids are shown in the middle sub-image, where only the overlapping portion of the projected grids is completely opaque, while adjacent regions above and below have an intermediate intensity as a result of overlap

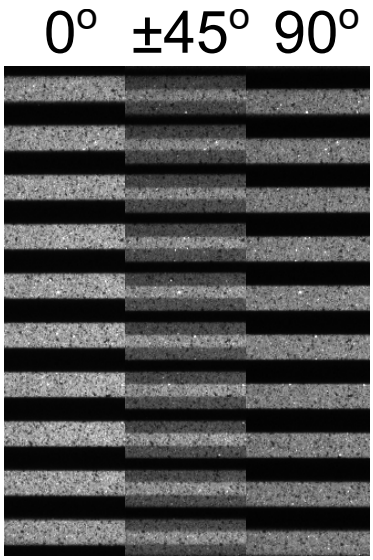


Figure 15: Projection of a Ronchi ruling through the backward-oriented RP-QQ onto a retroreflective background for three linear polarization azimuths incident on the prism.

between projected grids from both orthogonal polarization input states. For the focusing schlieren system described in [11], the input polarization state to the RP-QQ is always LVP, and so a sharp image of the Ronchi ruling is projected onto the retroreflective background, enabling the high-quality focusing and imaging capability of the system.

A final comment on the selection of an appropriate Rochon prism for use in focusing schlieren or other bi-directional imaging applications is warranted. At first, one may conclude after reading this manuscript that the optical activity of the quartz material in the RP-QQ prism results in unnecessarily complex intensity and polarization states at the output of the prism when used in the forward and backward directions, and that an alternative prism such as the RP-GQ or RP-MM described in this work would greatly simplify operation. However, a benefit of using the RP-QQ prism is that the optical activity associated with the quartz material when light propagates along its optic axis can eliminate the need for a quarter-wave plate in the focusing schlieren instrument. With the RP-GQ and RP-MM prisms, a quarter-wave plate is required to function as part of an optical isolator within the instrument that ultimately rotates the polarization state of light from LVP to LHP after light has been retroreflected (see [11] for a more detailed discussion). With the RP-QQ in the backward direction, the LVP light that initially enters the prism is output (completed unrefracted) with continuously-varying polarization state over the clear aperture. When this continuously-varying polarized light returns to the RP-QQ after retroreflection and passes through the prism in the forward orientation, the result is a continuously-varying transmitted power over the prism face B with both LVP and LHP polarization states. A linear polarizer can then be used to isolate only the LHP component and form a focused schlieren image with this light on the image sensor. Since the power in each LHP ray varies continuously after exiting prism face B in this forward direction, the resulting intensity recorded at a single point/pixel is the average power of each ray terminating at that point. The result is an image of relatively uniform intensity in the absence of any density or occluding object. This removes the need to include a large and costly quarter-wave plate in the focusing schlieren instrument, which improves its flexibility and reduces the mechanical and optical complexity. It should be noted, however, that as the structure angle is increased for the RP-QQ, the frequency of the polarization variation (in the backward orientation) and the intensity variation (in the forward orientation) decreases, resulting in a reduction in focused schlieren image quality if used without a quarter-wave plate.

# 6 Conclusions

Although polarizing prisms are generally used for laser beam polarization splitting applications, they have found use in imaging applications as well. Typically, the prisms are used in their forward (intended) orientation, but as demonstrated in a recently reported focusing schlieren system, light must pass in both the forward and backward direction for certain imaging techniques to properly function. In this study, three Rochon prisms (RP-QQ, RP-GQ, RP-MM) were characterized in terms

of their intensity and polarization state transmission characteristics, for both the unrefracted and refracted beams in the forward and backward orientation. Laser data along the height of the prisms were acquired with a polarimeter for precise power and polarization measurements, and these data were qualitatively validated with collimated LED light imaging over the entire clear aperture of the prisms.

With light passing through the RP-QQ in the forward direction, the projected intensity of both the unrefracted and refracted beams varied sinusoidally over the height of the prism for a single input plane polarization azimuthal orientation. The polarization state of the unrefracted beam was uniformly LVP light, while that of the refracted beam was uniformly LHP light. With light passing through the RP-QQ in the backward direction, the projected intensity of either the unrefracted or refracted beam was always uniform over the clear aperture, regardless of incident beam height. However, while the outgoing polarization state was always linear for this prism, its azimuth changed sinusoidally over the height of the prism. The sinusoidal variation of the intensity for the forward orientation and of the polarization for the backward orientation are due to the optical activity of the quartz material. From measurements in both directions, the specific rotation of quartz was measured for various wavelengths and compared favorably to existing data. From these results, the forward and backward orientations of the prism operate nearly inverse of each other for their transmitted power and polarization properties.

The RP-GQ and RP-MM described in this work operated the same in both the forward and backward orientations. Both the projected intensity and the transmitted polarization state were uniform over the entire clear aperture for both the unrefracted and refracted beams. The unrefracted beam maintained its LVP state, while the refracted beam maintained its LHP state. Due to a slight mismatch in index of refraction of glass and the o-ray index of refraction of quartz, the RP-GQ unrefracted beam was actually slightly refracted. This slight refraction can be eliminated either by selecting an exact index-matched glass for the appropriate wavelength of light used, or by selecting a material that does not experience optical activity (such as $MgF_2$) to fabricate both halves of the Rochon prism.

The use of the RP-QQ to project a Ronchi ruling grid onto a retroreflective background in a focusing schlieren system was demonstrated, where LVP light was transmitted through the prism in the backward orientation to project only the unrefracted light, resulting in a sharp projection of the grid which allows for the narrow depth-of-field focusing capability. While the RP-GQ and RP-MM are excellent options for the focusing schlieren system due to their orientation reciprocity, the non-ideal light propagation properties of the RP-QQ can make it a viable option in a focusing schlieren system to reduce both the overall number of optics required and the system's cost. The characterization of the three Rochon prisms in this study can be used as a reference for designs of future large clear aperture imaging system applications.

## References


1. Dennis F. Vanderwerf. Polarization Properties of Prisms and Reflectors. In *Applied Prismatic and Reflective Optics*, pages 61–96. SPIE, 2010.

2. Francis Hughes Smith. Interference Microscope, June 1952.

3. Delbert L. Lessor, John S. Hartman, and Richard L. Gordon. Quantitative surface topography determination by Nomarski reflection microscopy. I. Theory. *Journal of the Optical Society of America*, 69(2):357–366, February 1979.

4. Maksymilian Pluta. Nomarski's DIC microscopy: a review. In Maksymilian Pluta and Mariusz Szyjer, editors, *Phase Contrast and Differential Interference Contrast Imaging Techniques and Applications*. SPIE, May 1994.

5. Sonika Rathi, Nicholas Zoubek, Vivian J. Zagarese, and Daniel S. Johnson. Differential interference contrast microscopy with adjustable plastic Sanderson prisms. *Applied Optics*, 59(11):3404–3410, April 2020.

6. R. D. Small, V. A. Sernas, and R. H. Page. Single Beam Schlieren Interferometer Using a Wollaston Prism. *Applied Optics*, 11(4):858–862, April 1972.

7. A. Howard, D. Haberberger, R. Boni, R. Brown, and D. H. Froula. Implementation of a Wollaston interferometry diagnostic on OMEGA EP. *Review of Scientific Instruments*, 89(10):10B107, October 2018.

8. S. R. Sanderson. Simple, adjustable beam splitting element for differential interferometers based on photoelastic birefringence of a prismatic bar. *Review of Scientific Instruments*, 76(11):113703, November 2005.

9. Matthew M. Biss, Gary S. Settles, Matthew E. Staymates, and Simon R. Sanderson. Differential schlieren-interferometry with a simple adjustable Wollaston-like prism. *Applied Optics*, 47(3):328–335, January 2008.

10. Jennifer Schulz, Beric Skews, and Alessandro Filippi. Flow visualization using a Sanderson prism. *Journal of Visualization*, 22:1–13, September 2018.

11. Brett F. Bathel and Joshua M. Weisberger. Compact, self-aligned focusing schlieren system. *Optics Letters*, 46(14):3328, July 2021.

12. L. M. Weinstein. Review and update of lens and grid schlieren and motion camera schlieren. *The European Physical Journal Special Topics*, 182:65–95, July 2010.

13. Gary S. Settles and Michael J. Hargather. A review of recent developments in schlieren and shadowgraph techniques. *Measurement Science and Technology*, 28(4):042001, February 2017.

14. G. S. Settles. *Schlieren and Shadowgraph Techniques*. Springer Berlin Heidelberg, 2001.

15. E. O. Ammann and G. A. Massey. Modified Forms for Glan-Thompson and Rochon Prisms. *Journal of the Optical Society of America*, 58(11):1427–1433, November 1968.

16. Yu. V. Osipov. Noninvariance of interference of polarized waves at the exit of the Rochon birefringent prism. *Journal of Optical Technology*, 66(2):164, February 1999.

17. Francis A. Jenkins and Harvey E. White. *Fundamentals of Optics*. McGraw-Hill, New York, 2001.

18. Gorachand Ghosh. Dispersion-equation coefficients for the refractive index and birefringence of calcite and quartz crystals. *Optics Communications*, 163(1-3):95–102, May 1999.

19. Marilyn J. Dodge. Refractive properties of magnesium fluoride. *Applied Optics*, 23(12):1980–1985, June 1984.

20. S. Chandrasekhar. The optical rotatory power of quartz and its variation with temperature. *Proceedings of the Indian Academy of Sciences - Section A*, 35(3):103–113, March 1952.

21. Albert König. Angle-Measuring Appliance, U.S. Patent 942,393, October 1909.

22. Eugene O. Ammann. Optical Polarizing Prism, U.S. Patent 3,511,556, May 1970.

23. E. O. Ammann and G. A. Massey. Less-Expensive Rochon Prisms. Technical Report 70-10681, NASA, December 1970.

| REPORT DOCUMENTATION PAGE | Form Approved OMB No. 0704–0188 |
|---|---|



| 1. REPORT DATE *(DD-MM-YYYY)* | 2. REPORT TYPE | 3. DATES COVERED *(From - To)* |
|---|---|---|
| 01-01-2022 | Technical Memorandum | |

**4. TITLE AND SUBTITLE**
Characterization of Rochon Prisms for Bi-Directional Imaging Applications

**5a. CONTRACT NUMBER**

**5b. GRANT NUMBER**

**5c. PROGRAM ELEMENT NUMBER**

**6. AUTHOR(S)**
Joshua M. Weisberger and Brett F. Bathel

**5d. PROJECT NUMBER**

**5e. TASK NUMBER**

**5f. WORK UNIT NUMBER**
109492.02.07.05.06

**7. PERFORMING ORGANIZATION NAME(S) AND ADDRESS(ES)**
NASA Langley Research Center
Hampton, Virginia 23681-2199

**8. PERFORMING ORGANIZATION REPORT NUMBER**

**9. SPONSORING/MONITORING AGENCY NAME(S) AND ADDRESS(ES)**
National Aeronautics and Space Administration
Washington, DC 20546-0001

**10. SPONSOR/MONITOR'S ACRONYM(S)**
NASA

**11. SPONSOR/MONITOR'S REPORT NUMBER(S)**
NASA/TM–20210026232

**12. DISTRIBUTION/AVAILABILITY STATEMENT**
Unclassified-Unlimited
Subject Category 35
Availability: NASA STI Program (757) 864-9658

**13. SUPPLEMENTARY NOTES**
An electronic version can be found at http://ntrs.nasa.gov.

**14. ABSTRACT**
Polarizing prisms are often used in applications where light is split into two separate beams of orthogonal polarization, or to isolate a beam with a preferred polarization state. These prisms are typically used with lasers, but there are applications of their use with imaging systems. One such example is that of a recently developed focusing schlieren system, where light must be transmitted through a Rochon prism in both the forward and backward directions. Three Rochon prisms were characterized in this study in terms of their transmitted intensity and polarization state: a quartz/quartz prism, a glass/quartz prism, and a MgF2/MgF2 prism. Laser testing at four wavelengths was performed, along with full clear aperture collimated LED light testing at a single wavelength. The glass/quartz and MgF2/MgF2 prisms operated in the same manner when light was transmitted in either the forward or backward direction. The quartz/quartz prism, however, exhibited differences between operation in the forward and backward direction.

**15. SUBJECT TERMS**
Polarizing,Prism,Imaging

| 16. SECURITY CLASSIFICATION OF: | | | 17. LIMITATION OF ABSTRACT | 18. NUMBER OF PAGES | 19a. NAME OF RESPONSIBLE PERSON |
|---|---|---|---|---|---|
| a. REPORT | b. ABSTRACT | c. THIS PAGE | | | STI Information Desk (help@sti.nasa.gov) |
| U | U | U | UU | 31 | 19b. TELEPHONE NUMBER *(Include area code)* (757) 864-9658 |